

Multi-beam OCT imaging based on an integrated, free-space interferometer

YONGJOO KIM,^{1,2,*}  NORMAN LIPPOK,^{1,2} AND BENJAMIN J. VAKOC^{1,2,3}

¹Wellman Center for Photomedicine, Massachusetts General Hospital, 40 Blossom St., Boston, MA 02114, USA

²Harvard Medical School, 25 Shattuck Street, Boston, MA 02115, USA

³Harvard-MIT Division of Health Sciences and Technology, Cambridge, MA 02139, USA

*ykim60@mgh.harvard.edu

Abstract: While it is a common practice to increase the speed of swept-source optical coherence tomography (OCT) systems by using a high-speed source, this approach may not always be optimal. Parallelization in the form of multiple imaging beams is an alternative approach, but scalable and low-loss multi-beam OCT architectures are needed to capitalize on its advantages. In this study, we demonstrate an eight-beam OCT system using an interferometer architecture comprising planar lightwave circuits (PLC) splitters, V-groove assemblies (VGA), and optical ribbon fibers. We achieved an excess loss and heterodyne efficiency on each channel that was close to that of single-beam systems. *In vivo* structural imaging of a human finger and OCT angiography imaging of a mouse ear was performed to demonstrate the imaging performance of the system. This work provides further evidence supporting multi-beam architectures as a viable strategy for increasing OCT imaging speed.

© 2020 Optical Society of America under the terms of the [OSA Open Access Publishing Agreement](#)

1. Introduction

Swept-source optical coherence tomography (OCT)/optical frequency domain imaging (OFDI) systems can be implemented to illuminate the sample with either a single beam, or with multiple beams. In the former, which is more common, the single beam is raster scanned across the sample. This approach has the advantage of simplicity, needing only a single sample arm path in the interferometer. An optical circulator can be used to efficiently direct light to the sample and return scattered light to the mixing optics. Because this mixing is between two single-mode fibers, a high heterodyne efficiency can be obtained [1,2]. These features allow single-beam systems to achieve high-sensitivity imaging.

However, as systems evolve toward megahertz-scale imaging speeds, the limitations of the single-beam approach become apparent. First, there are limited laser source technologies capable of operating at megahertz-scale speeds [3], and those that do suffer from performance, cost, or stability penalties relative to slower source technologies. Second, a MHz-scale single-beam OCT system requires high-resolution (i.e., a large number of resolvable points) and high-speed beam scanning. This can preclude galvanometric scanners, forcing use of more restrictive resonant scanners or polygon-scanning mirrors [4]. Finally, to mitigate the intrinsic sensitivity penalties of higher-speed imaging, higher imaging powers may need to be used [5,6]. While this is true for both single and multi-beam systems, a high-power single-beam system would concentrate this light into a single focused spot, raising potential safety concerns.

Each of these challenges can be mitigated by use of a multi-beam system. In a multi-beam system, the system imaging speed is the product of the source speed and the number of beams. As such, slower source technologies can be used. Each beam within a multi-beam system needs to acquire a subset of the overall field, reducing the scan engine speed and/or resolution

requirements. Finally, spreading the imaging power across multiple, separated spots creates a more favorable safety profile.

OCT architectures that scale to larger beam counts, induce minimal excess loss, and support high heterodyne efficiency will be key to making multi-beam approaches feasible. Most prior implementations of multi-beam OCT are deficient in one or more of these areas. Multiple approaches have been demonstrated with passive optical splitters located in a bi-directional path of the sample arm [7,8]. This, of course, induces a significant loss in the return path, resulting in a sensitivity penalty that increases with channel count. More power-efficient approaches have been demonstrated by using separate interferometers for each beam [9–12], but these approaches are difficult to scale to larger beam counts.

Here, we sought a multi-beam interferometer architecture that is scalable, provides low excess loss, and achieves a high heterodyne efficiency. We demonstrate an 8-beam approach based on inexpensive photonic devices including planar lightwave circuit (PLC) splitters and V-groove assemblies (VGA). A free-space multi-beam sample arm/multi-beam reference arm mixing beamsplitter was implemented. The system was operated with a 125 kHz swept-source laser, resulting in a 1 MHz system A-line rate. The penalty due to coupling loss and degraded modal overlap in the multi-beam heterodyne mixer resulted in an SNR penalty of approximately 3.4 dB relative to an all-fiber, single-beam interferometer and less than 3 dB relative to a single-beam interferometer using a free-space heterodyne mixer. We used this system to acquire structural images of human skin, and to perform angiographic imaging in a mouse ear. For each, the sub-field images from each beam were fused to generate gap-free volumetric datasets devoid of stitch artifacts. While this first design used polarization to efficiently couple reflected light from the sample to the mixing beamsplitter, and as a result did not support polarization diverse imaging, the promising results nonetheless suggest that multi-beam architectures should be explored alongside MHz-speed laser development as a strategy for increasing the speed of OCT.

2. Methods

2.1. Multi-beam OCT system

Figure 1(A) presents the multi-beam OCT system setup. A custom-built wavelength-swept laser incorporating a tunable Fabry-Perot filter (Micron Optics Inc) driven at 62.5 kHz and a semiconductor optical amplifier (SOA; Thorlabs) was used as a light source centered at 1300 nm [13]. The SOA was modulated with a 50% duty cycle and an external-cavity buffer was used to provide an A-line rate of 125 kHz. An additional SOA was used to boost the output power to give 60 mW output power. Two percent of the laser output was tapped and half of the tapped light was sent to a fiber Bragg grating (O/E land) that has a narrow reflection bandwidth at 1300 nm to generate an A-line trigger. The other half was directed to a Mach-Zehnder interferometer (MZI) with a 1 mm path-mismatch in order to generate a calibration vector for linear k -space resampling. The remaining 98% of the output was delivered to the multi-beam OCT interferometer and split into the reference and sample arms using a 20/80 fiber-optic coupler. In the reference arm, a 1x8 PLC splitter (Fiberstore)

was used to divide the input into an 8-fiber ribbon cable. The terminal of the fiber ribbon was unconnectorized and spliced to another 8 single-mode optical fiber ribbon that was pigtailed to a VGA (OZ Optics) using a ribbon fusion splicer (Fujikura). In the VGA, the 8 fiber channels were arranged linearly with 250 μm spacing.

In the same manner, a 1x8 PLC was used in the sample arm, coupled to a ribbon fiber and VGA. The 8 fields at the end face of the VGA were relayed by the multi-beam microscope creating 8 focal spots displaced by 850 μm on the sample plane. The microscope design, which will be further discussed in the following subsection, was optimized using ray-tracing software (Zemax, LLC). In simulation, diffraction-limited focal spots were achieved over a 6.8 x 6.8 mm field-of-view. The polarization controller before the PLC in the sample arm was configured to

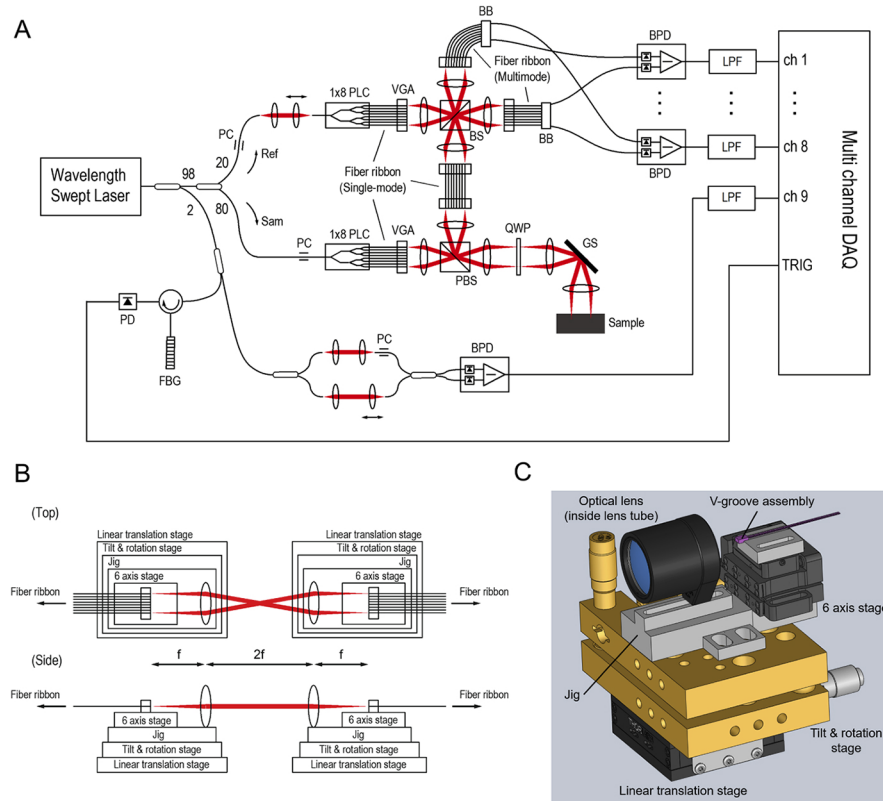


Fig. 1. Multi-beam OCT system. (A) A schematic drawing of the multi-beam OCT system. BB: Breakout box, BS: Beam splitter, BPD: Balanced photodetector, FBG: Fiber bragg grating, GS: Galvo scanner, LPF: Low pass filter, PBS: Polarizing beam splitter, PC: Polarization controller, PD: Photodetector, PLC: Planar lightwave circuit, QWP: Quarter wave plate, VGA: V-groove assembly. (B) Free-space multi-beam alignment. For simplicity, only the optical beams launched off and into both edges of the VGA are illustrated. (C) CAD (Solidworks) design of the alignment unit used to construct the multi-beam heterodyne mixing optics.

align the polarization states of the illumination beams to maximize transmission through the polarization beam splitter (PBS) in the microscope. Double passing through the quarter-wave plate (QWP) orthogonalized the returned light polarization state, which routed the reflections to an additional single-mode fiber ribbon. This ribbon fiber delivered the reflected light to the heterodyne mixing optics.

In the heterodyne mixer, each of the 8 reference and sample fields arrive at the interfering beamsplitter (BS), created 8 interference fringes at each of two output ports. Multimode 8-fiber ribbon cables collected these interference beams with high coupling efficiency and conveyed them to 8 balanced photodetectors (Thorlabs). The resulting fringe signals were digitized on the first 8 channels of a 16-channel data acquisition board (14 bit, 100 MS/s per channel; AlazarTech). The MZI k -space linearizing signal was acquired on the ninth digitizer channel.

2.2. Free-space multi-beam alignment

Optimal alignment between the VGAs in both the microscope and the heterodyne mixer is critical to achieving low loss and high heterodyne efficiency across all 8 channels. In Fig. 1(B), the

alignment units holding the VGA, optical lens, and kinematic stages are illustrated. The 6-axis stage (Newport) holding the VGA controls the relative position (x , y , z) and angle (yaw, pitch) with respect to the optical lens (Thorlabs), providing 8 collimated beams whose aperture stop was located at one focal length distance away from the lens. By controlling the roll of the stage, one can match the V-groove axes - imaginary lines that intersect the fiber cores at the end faces of the illuminating and receiving VGAs. The alignment between the 6-axis stage and the lens was secured on a custom-designed jig, which was mounted on the tilt and rotation stage (Newport). The manipulation of the tilt and rotation stages allows a global alignment of the 8 beams. The linear translation stage (Thorlabs) was used to set the distance between the lenses to twice the focal length so that the 8 fiber channels on the illumination side can be imaged and coupled to that on the receiving side. An isometric view of an alignment unit in SolidWorks software (Dassault Systemes) is shown in Fig. 1(C).

2.3. Microscope design

In Fig. 2(A), we present the ray-tracing model of the multi-beam microscope. The PBS and QWP are not included in these simulations for simplicity. Two critical parameters characterizing the microscope are the beam spacing on the sample and the focal spot size on the sample. Denoting the fiber spacing in the VGA as d , the sample beam spacing is set by the magnifications of the two telescopes (L1:L2 and L3:L4), given as

$$\text{Beam spacing} = \frac{f_2 f_4}{f_1 f_3} d \quad (1)$$

where f_1, f_2, f_3 , and f_4 are the focal lengths of L1, L2, L3, and L4, respectively. The focal spot size is determined by the beam size incident on L4 and the focal length of L4. The beam size after L1 is $2DAf_1$, in which DA is the divergence angle of the light exiting the single-mode fiber at the VGA end face. After passing L2 and L3, the beam expands by a factor of f_3/f_2 and the beam size on the galvo and, correspondingly, the beam size incident on L4 is $2DAf_1 f_3/f_2$, resulting in the focal spot size on the sample.

$$\text{Focal spot size} = \frac{2\lambda f_2 f_4}{\pi DA f_1 f_3} \quad (2)$$

Optical aberrations can degrade the achievable spot size, especially for beams launched from the perimeter fibers in the VGAs. Using ZEMAX, we optimized the microscope design to minimize these aberrations. Figure 2(B) shows the optical layout of the microscope in ZEMAX. Note that this resulted in the use of a pair of achromatic doublet lenses for L1, L2, and L4. Similar to prior reports [14], we found that combining multiple lenses of lower refractive power reduced aberrations relative to a single lens design. In Fig. 2(C), the 8 focal spots were simulated at three wavelengths (one from the central wavelength and two from the maximum and minimum wavelengths of the source spectrum) and at three different locations in the fast-axis direction to include galvanometer scanning. In all of the 24 locations, the focal spots were smaller than the Airy disks, which are indicated by the black solid circles with a radius of 28.25 μm . This confirms that the aberration in the microscope is sufficiently corrected and diffraction-limited spots are achieved across the imaging field [15]. The imaging parameters are summarized in Table 1.

2.4. Fringe visibility measurement

The free-space heterodyne mixer uses multi-mode optical fibers at the output to simplify alignment and relax alignment tolerances. As such, the performance of the mixer cannot be captured solely by the power coupling efficiency from the single-mode to multimode fibers in the sample

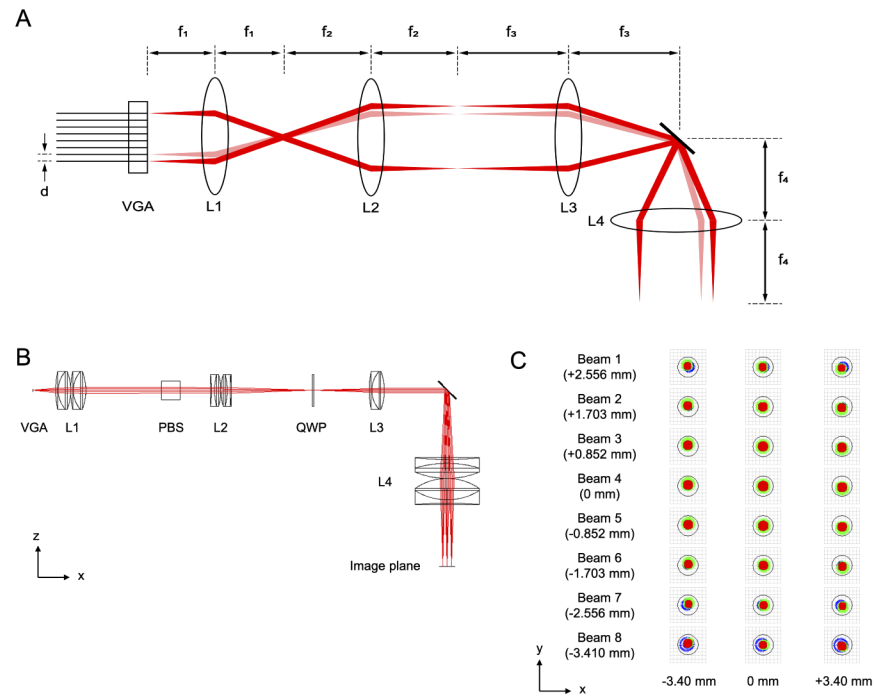


Fig. 2. Multi-beam microscope. (A) A schematic drawing of the multi-beam microscope illustrating beam relay from a VGA to an image plane. (B) Optical layout of the microscope generated in ZEMAX. (C) Spot diagrams at different locations on imaging field-of-view. The blue, red, and green indicates the spot diagrams at 1240, 1300, and 1360 nm, respectively. The Airy disks at 1240 nm are shown as black circles.

Table 1. Imaging Parameters

Imaging parameters		
Fiber spacing (d)		250 μm
Effective focal lengths	Lens 1 (f_1)	27.0 mm
	Lens 2 (f_2)	72.5 mm
	Lens 3 (f_3)	50.1 mm
	Lens 4 (f_4)	63.4 mm
Beam size on galvo mirror		3.40 mm
Beam spacing		0.85 mm
Focal spot size		31.1 μm

arm; a second parameter describing the modal overlap between the reference and sample arm at the interfering beam splitter is needed. Heterodyne efficiency is a common parameter used to quantify modal overlap [16–18]. To measure heterodyne efficiency, we measured the fringe visibility of each beam. The process for measuring fringe visibility was as follows: first, an optical trace of the reference arm light on one output port was acquired with the sample arm blocked ($I_R(k)$); next, a sample arm trace was recorded from the same output port with the reference arm blocked ($I_S(k)$); finally, an interference fringe on the same output port was acquired (unblocked sample and reference arm, $I(k)$). The upper and lower envelopes ($I_{\text{upper/lower}}(k)$) were calculated by interpolating local maxima and minima of the interference fringe $I(k)$, respectively. (Fig. 3(A))

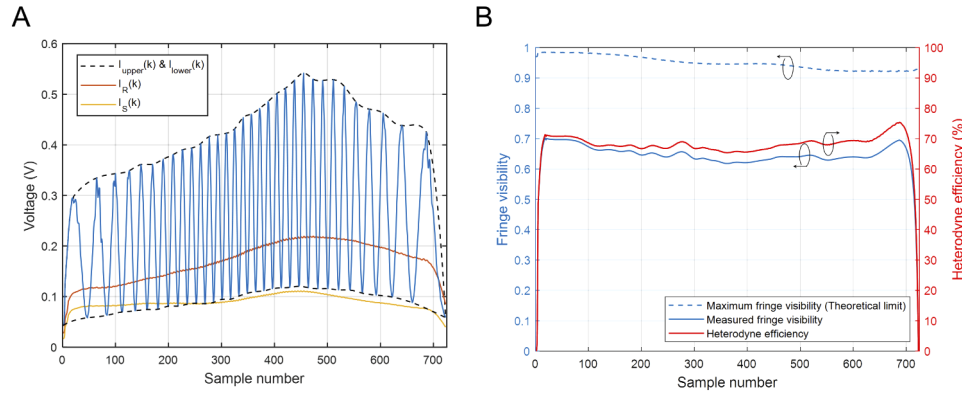


Fig. 3. Fringe visibility and heterodyne efficiency measurement. (A) An OCT interferogram (blue solid line) demarcated by the upper and lower envelopes (black dotted lines). The reference (red solid line) and sample (orange solid line) arm traces are measured separately. (B) Measured and maximum fringe visibilities (left y-axis) and heterodyne efficiency (right y-axis) as a function of wavenumber.

The measured fringe visibility was calculated as

$$\mathcal{V}_{\text{measured}}(k) = \frac{I_{\text{upper}}(k) - I_{\text{lower}}(k)}{I_{\text{upper}}(k) + I_{\text{lower}}(k)} \quad (3)$$

and the maximum fringe visibility was calculated as

$$\mathcal{V}_{\text{max}}(k) = \frac{2\sqrt{I_R(k)I_S(k)}}{I_R(k) + I_S(k)} \quad (4)$$

and the heterodyne efficiency was calculated as $\mathcal{V}_{\text{measured}}(k)/\mathcal{V}_{\text{max}}(k)$.

In Fig. 3(B), the measured and maximum fringe visibilities and heterodyne efficiency are plotted as a function of wavenumber. The average heterodyne efficiency was calculated within a 10-90% range across wavenumber.

We note that the heterodyne efficiency is also affected by the degree of polarization alignment and the source coherence length relative to the group delay mismatch between interfering beams, neither of which are properties of the multi-beam heterodyne mixer. To remove the contributions from these sources, we measured the heterodyne efficiency of a single-beam, all-fiber mixer using the same methodology, the same source, and with signals at the same depth location. This gave a baseline heterodyne efficiency of 87%.

2.5. Image processing and registration

A calibration vector generated by the MZI signal was used for k -space resampling in each data channel. A quadratic phase curve was applied to interferograms in each channel to numerically compensate dispersion mismatch between the reference and sample arms [19]. For OCTA imaging, 5 repeated B-scans (500 A-scans/B-scan) were acquired at each of 70 B-scan locations (per channel), resulting in 1.68 seconds of total data acquisition time (including an additional 100 A-scans/B-scan for galvanometer swing-back time). Within each pair of the repeated B-scans, a post-processing motion compensation algorithm was applied [20], after which a complex-differential variance algorithm was used to generate an OCTA B-scan [21]. A total of 8 maximum projection *en face* OCTA images (500 pixels x 70 pixels) was generated, each spanning 6.8 mm in the fast-axis direction and 0.95 mm in the slow-axis direction.

The 8 OCTA images capture different sub-fields and require an image registration process to generate a merged dataset spanning the full field. For a given scanning protocol, the relative position of an *en face* image with respect to the neighboring *en face* image remains constant, therefore the image registration parameters can be solved for once and reused for subsequent imaging experiments, assuming the microscope is not reconfigured. For this purpose, a grid test target (Thorlabs) was imaged. Since each sub-field has a larger imaging field-of-view in the slow-axis direction (0.95 mm) than the beam spacing set by the microscope (0.85 mm), there are ~10% overlaps between each pair of neighboring *en face* intensity projection images and sub-pixel image shifts in both fast and slow axis direction that maximize the cross-correlation within each overlap were found using the same algorithm that was used for motion compensation. These were used as *a priori* information for registering volumetric structure images and *en face* OCTA images, thereafter.

2.6. Animal protocol

OCTA imaging was performed in a mouse ear vasculature to validate the imaging performance of the system. A BALB/c mouse was anesthetized with inhalation of isoflurane (2.5% for induction and 1.5% for maintenance) and depilatory cream was applied to the ear skin for 5 minutes. After wiping out the cream, the ear skin was gently placed in contact with an optical imaging window (Thorlabs) to aid positioning of the tissue and to minimize the sample motion. The animal experiment was approved and conducted in accordance with Institutional Animal care and Use Committee (IACUC) at Massachusetts General Hospital.

3. Results

3.1. System parameter measurements

Table 2 summarizes the measured parameters of each channel. For the measurements, a 47.2 dB attenuator was included before the PLC splitter in the sample arm and a mirror working as a single reflector for each channel was placed in the focal plane of the microscope. The zero-depth positions were measured in all 8 channels and the differences of the position of each channel to that of channel 1 were calculated as the path-length difference in the first row. The path-length differences are attributed to the non-uniform fiber lengths in the ribbon and different optical path-length for each beam to travel in the microscope. The maximum path-length difference was 205 μm , which is one order of magnitude smaller than the ranging depth of the system.

The heterodyne efficiency in each channel was measured when the reference and sample arm powers were 10 μW and 2 μW respectively, and the path-mismatch was 500 μm . The average heterodyne efficiency averaged across the channels was 65%, resulting in an average SNR degradation (relative to 100% heterodyne efficiency) of 3.74 dB. As noted in Section 2.4, the baseline heterodyne efficiency was 87% (due to laser coherence length and polarization misalignment), resulting in a corresponding SNR degradation of 1.21 dB. Thus, the SNR penalty

Table 2. Path-length variation, fringe visibility, sensitivity measurement

Channel	1	2	3	4	5	6	7	8
Path-length difference relative to channel 1 (μm)	-	110	90	110	135	150	205	90
Heterodyne efficiency (%)	61.9	67.7	66.0	64.1	63.4	65.0	63.9	67.8
Sensitivity (dB)	91.3	93.3	91.0	93.2	93.3	93.0	93.0	92.6
Maximum sensitivity (dB)	93.0	93.9	93.6	93.6	93.5	93.7	93.3	93.1

due to the multi-beam heterodyne mixer is 2.53 dB ($= 3.74 \text{ dB} - 1.21 \text{ dB}$). The excess loss of the heterodyne mixer was 0.86 dB (82% power transmission). Thus, the total SNR penalty of the multi-beam heterodyne mixer relative to a single-beam, all-fiber mixer was 3.39 dB ($= 2.53 \text{ dB} + 0.86 \text{ dB}$), and the SNR penalty relative to a single-beam, free-space mixer was 2.53 dB (assuming similar 0.86 dB fiber to fiber excess loss). Although the efficiencies were observed to be uniform within $\pm 3\%$ margin, the values were less than 100%. This could be a result of sub-optimal alignment between the reference and sample fields due to inaccurate VGA manufacturing, imperfect polarization alignment between the reference and sample arm, and finite laser coherence lengths. Single-beam systems in theory can achieve 100% heterodyne efficiency, but in practice are degraded by the aberration effects resulting from multi-beam optics.

The coupling efficiency of the reflected beams from the microscope was 68.5% and the system sensitivities were $92.13 \pm 1.13 \text{ dB}$ at 3.7 mW average power incident on the sample in each channel. The sensitivity variation between the channels is due in large part to polarization dispersion in the fiber ribbon [22], resulting in channel-dependent polarization mismatch between the reference and sample fields. The maximum sensitivities were obtained after optimizing the polarization controller in the sample arm for each channel and are presented in the fourth row of Table 2. The maximum sensitivities were $93.45 \pm 0.31 \text{ dB}$, indicating that the sensitivity penalty arising from polarization effects was $\sim 1.3 \text{ dB}$. Note that the measured maximum sensitivity is $\sim 13 \text{ dB}$ lower than the theoretical shot-noise limited sensitivity. This difference is due to the excess loss in the microscope (1.64 dB), the excess loss in the heterodyne mixer (0.86 dB), and the SNR degradation due to 65% heterodyne efficiency (3.74 dB). The laser RIN, the optical power imbalance in the balanced detection, and the effect of a post-processing window can further limit the measured sensitivity from its theoretical value [13].

3.2. Human finger structural imaging

Figure 4 shows *in vivo* structural images of a human finger. In Fig. 4(A), each of the 8 volumetric images was shifted axially by its path-length difference measured in Table 2 and registered to generate a merged volumetric image. The representative cross-sectional images from each channel are shown in Fig. 4(B).

3.3. Mouse ear OCTA imaging

Figure 5 shows OCTA images acquired from the mouse ear vasculature. The 8 OCTA images on the left were registered and generated the composite OCTA image on the right showing good blood vessel continuity and global image contrast. In either flank of the composite image, there are wedge-like features pointing upward and downward, which is a consequence of the accumulated image displacement along the fast axis direction during the image registration. The maximum image displacement is $\sim 100 \mu\text{m}$.

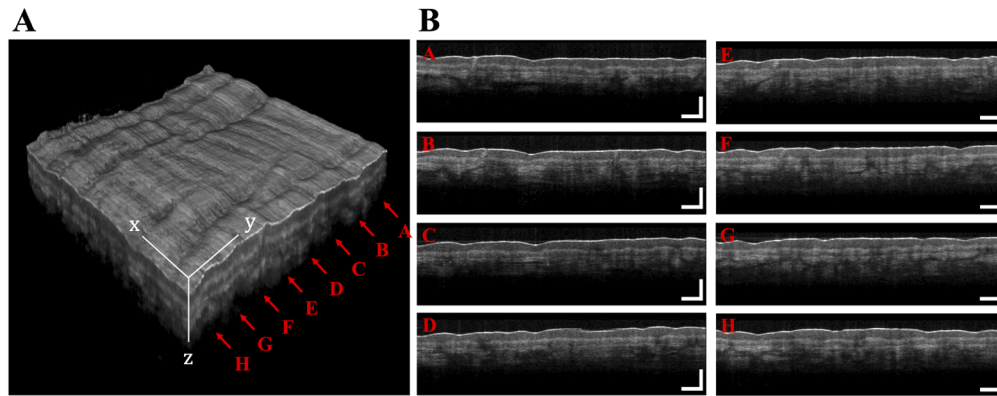


Fig. 4. Structural images of a human finger. (A) A 3D visualization of the merged volumetric image. The red arrows and corresponding letters indicate locations where cross-sectional (x-z) images from each channel were acquired. (B) Representative cross-sectional images from each channel. Scale bars: 500 μm .

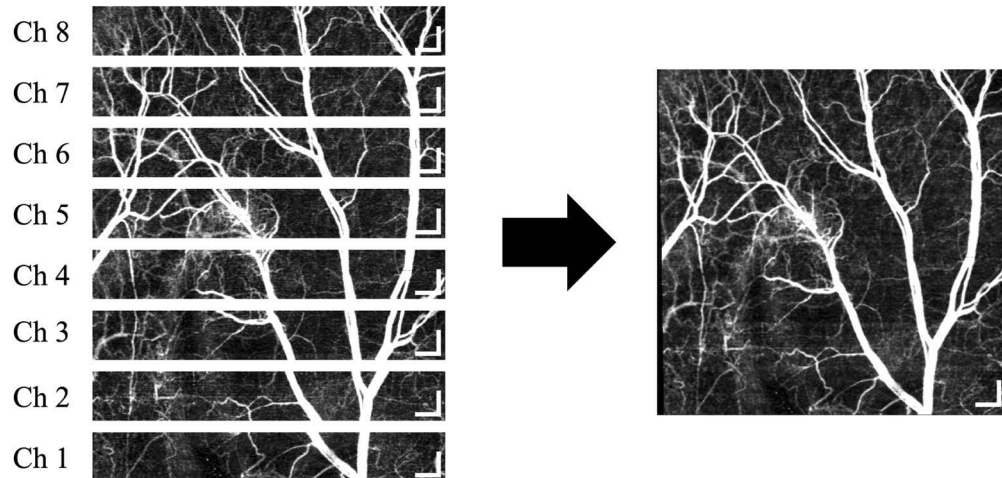


Fig. 5. OCTA imaging of the mouse ear vasculature. (Left) OCTA images acquired from each channel. (Right) A composite OCTA image after image registration. Scale bars: 500 μm .

4. Conclusion and discussion

We demonstrated multi-beam OCT imaging at 1 MHz system A-scan rate using a 125 kHz laser with 8 imaging beams. The *in vivo* imaging results and measured performance demonstrate that the excess loss and heterodyne efficiency are only slightly affected by the multi-beam architecture. The architecture is in principle scalable to higher beam counts, with optical aberration likely being the ultimate limit to the channel count.

We note here that this design required an 8-channel digitizer, but that the digitization rate of each channel is 1/8th that of a single-beam system with equivalent system speed. Further, we note that digitizer cost is primarily a function of the total digitized signal bandwidth, and the need to create a larger number of slower digitizer channels is not likely to be a significant detractor.

Finally, this architecture can be improved by supporting polarization-diverse detection, which would likely require an alternative, non-polarizing approach for coupling light to/from the sample

arm. High-power sources that maintain 20-30 mW imaging power in each beam are also needed to take advantage of the potential of multi-beam systems. Furthermore, all-fiber implementations that capture the benefits of the multi-beam approach without the complexity of free-space alignment could dramatically enhance the utility. Advances in these areas would further position multi-beam imaging as an alternative to single-beam systems for rapid OCT imaging.

Funding

U.S. Department of Defense (FA9550-11-1-0331); National Institutes of Health (P41EB015903).

Disclosures

The authors declare no conflicts of interest.

References

1. S. C. Cohen, "Heterodyne detection: phase front alignment, beam spot size, and detector uniformity," *Appl. Opt.* **14**(8), 1953–1959 (1975).
2. D. K. Jacob, M. B. Mark, and M. Bradley D. Duncan, "Heterodyne ladar system efficiency enhancement using single-mode optical fiber mixers," *Opt. Eng.* **34**(11), 3122 (1995).
3. T. Klein and R. Huber, "High-speed oct light sources and systems," *Biomed. Opt. Express* **8**(2), 828 (2017).
4. T. S. Kim, J. Joo, I. Shin, P. Shin, W. J. Kang, B. J. Vakoc, and W.-Y. Oh, "9.4 mhz a-line rate optical coherence tomography at 1300 nm using a wavelength-swept laser based on stretched-pulse active mode-locking," *Sci. Rep.* **10**, 9328 (2020).
5. K. Goda, A. Fard, O. Malik, G. Fu, A. Quach, and B. Jalali, "High-throughput optical coherence tomography at 800 nm," *Opt. Express* **20**(18), 19612–19617 (2012).
6. J. Xu, X. Wei, L. Yu, C. Zhang, J. Xu, K. K. Y. Wong, and K. K. Tsia, "Megahertz all-optical swept-source optical coherence tomography based on broadband amplified optical time-stretch," *Opt. Express* **39**(3), 622–625 (2014).
7. C. Zhou, A. Alex, J. Rasakanthan, and Y. Ma, "Space-division multiplexing optical coherence tomography," *Opt. Express* **21**(16), 19219–14704 (2013).
8. Y. Huang, M. Badar, A. Nitkowski, A. Weinroth, N. Tansu, and C. Zhou, "Wide-field high-speed space-division multiplexing optical coherence tomography using an integrated photonic device," *Biomed. Opt. Express* **8**(8), 3856–14704 (2017).
9. Y. Luo, L. J. Arauz, J. E. Castillo, J. K. Barton, and R. K. Kostuk, "Parallel optical coherence tomography system," *Appl. Opt.* **46**(34), 8291–14704 (2007).
10. B. Potsaid, B. Baumann, D. Huang, S. Barry, A. E. Cable, J. S. Schuman, J. S. Duker, and J. G. Fujimoto, "Ultrahigh speed 1050nm swept source/Fourier domain OCT retinal and anterior segment imaging at 100,000 to 400,000 axial scans per second," *Opt. Express* **18**(19), 20029–14704 (2010).
11. W. Wieser, B. R. Biedermann, T. Klein, C. M. Eigenwillig, and R. Huber, "Multi-Megahertz OCT: High quality 3D imaging at 20 million A-scans and 4.5 GVoxels per second," *Opt. Express* **18**(14), 14685–14704 (2010).
12. M. K. K. Leung, A. Mariampillai, B. A. Standish, K. K. C. Lee, N. R. Munce, I. A. Vitkin, and V. X. D. Yang, "High-power wavelength-swept laser in Littman telescope-less polygon filter and dual-amplifier configuration for multichannel optical coherence tomography," *Opt. Lett.* **34**(18), 2814–14704 (2009).
13. C. Jun, M. Villiger, W.-Y. Oh, and B. E. Bouma, "All-fiber wavelength swept ring laser based on Fabry-perot filter for optical frequency domain imaging," *Opt. Express* **22**(21), 25805–14704 (2014).
14. J. P. Kolb, T. Klein, C. L. Kufner, W. Wieser, A. S. Neubauer, and R. Huber, "Ultra-widefield retinal MHz-OCT imaging with up to 100 degrees viewing angle," *Biomed. Opt. Express* **6**(5), 1534–14704 (2015).
15. D. J. Brady and N. Hagen, "Multiscale lens design," *Biomed. Opt. Express* **17**(13), 10659–10674 (2009).
16. R. Frehlich, "Heterodyne efficiency for a coherent laser radar with diffuse or aerosol targets," *J. Mod. Opt.* **41**(11), 2115–2129 (1994).
17. M. Salem and J. P. Rolland, "Heterodyne efficiency of a detection system for partially coherent beams," *J. Opt. Soc. Am. A* **27**(5), 1111–1119 (2010).
18. Y. Ren, A. Dang, L. Liu, and H. Guo, "Heterodyne efficiency of a coherent free-space optical communication model through atmospheric turbulence," *Appl. Opt.* **51**(30), 7246 (2012).
19. M. Wojtkowski, V. J. Srinivasan, T. H. Ko, J. G. Fujimoto, A. Kowalczyk, and J. S. Duker, "Ultrahigh-resolution, high-speed, Fourier domain optical coherence tomography and methods for dispersion compensation," *Opt. Express* **12**(11), 2404–14704 (2004).
20. M. Guizar-Sicairos, S. T. Thurman, and J. R. Fienup, "Efficient subpixel image registration algorithms," *Opt. Express* **33**(2), 156–158 (2008).
21. A. S. Nam, I. Chico-Calero, and B. J. Vakoc, "Complex differential variance algorithm for optical coherence tomography angiography," *Biomed. Opt. Express* **5**(11), 3822–3832 (2014).
22. A. Galtarossa, C. G. Someda, A. Tommasini, B. A. Schrefler, G. Zavarise, and M. Schiano, "Stress Distribution in Optical-Fiber Ribbons," *IEEE Photonics Technol. Lett.* **9**(3), 354–356 (1997).